Computational Particle Mechanics manuscript No.
(will be inserted by the editor)

Explicit meshfree $u - p_w$ solution of the dynamic Biot formulation at large strain

Pedro Navas · Miguel Molinos · Miguel M. Stickle · Diego Manzanal · Angel Yagüe · Manuel Pastor

Received: date / Accepted: date

Abstract In this paper an efficient and robust methodology to simulate saturated soils subjected to low frequency dynamic loadings under large deformation regime is presented. The coupling between solid and fluid phases is solved through the dynamic reduced formulation of the Biot's equations. The additional novelty lies in the employment of an explicit time integration scheme of the $u - p_w$ (solid displacement – pore water pressure) formulation which enables us to take advantage of such explicit schemes. Shape functions based on the elegant Local Maximum Entropy approach, through the framework of Optimal Transportation Meshfree schem, are utilized to solve fluid saturated dynamic problems.

Keywords Biot's equations · Meshfree · Newmark Predictor-Corrector · Explicit approach · Large strains

1 Introduction

Modeling saturated soils under dynamic loads is an interesting issue, particularly when dynamic consolidation or quick settlements of soils under large deformations are concerned. However, the research focused on this aspect is scant, the literature being even more limited when finite deformations are involved. This is mainly due to the fact that, on the one hand, the $u - p_w$ (solid displacement – fluid pressure) formulation is widely used in dynamics to solve the coupled problem due to its simplicity (e.g. [6,34,35]), and on the other hand, since fluid accelerations are neglected in this formulation, this makes it impossible to capture high frequency movements when the coupling between soil and water needs to be dealt with [36].

Along the years, depending on the employed formulation for coupled problems (either simplified or complete), on the assumptions (if the accelerations are considered or not) and on the way that the equations are solved (explicit or implicit), different techniques to solve the coupled problem have been developed. The governing equations of the coupled problem were first introduced by Biot [?], then reviewed by Zienkiewicz and co-workers [35–37,34]. There were two alternatives to achieve the same set of equations: one by Zienkiewicz, Chang and Bettes [36], or Zienkiewicz and Shiomi [37, 34] applied at macroscopic scale, the other by Lewis and Schrefler [13] within the Hybrid Mixture Theory starting from the microscopic scale. Both showed that an accurate enough solution can be achieved for low frequency dynamic problems by neglecting the convective and acceleration terms in the complete formulation, deriving the $u - p_w$ formulation.

Regarding the application of $u - p_w$ formulation under large deformation regime, the first works were carried out by Diebels and Ehlers [10], Borja *et al.* [4,5] and Armero [1] who tested their models by simulating the constitutive behavior of the the solid phases with linear elastic, Cam-Clay and Drucker-Prager theories respectively. Around the same period of time, Ehlers and Eipper [11] applied a new Neo-Hookean constitutive model to represent the compaction of the soil up to the solid compaction point. All of these researches were solved using implicit schemes where the linearization of

P. Navas, D. Manzanal and A. Yagüe
Dep. Continuum Mechanics and Theory of Structures, Technical Univ. of Madrid
E-mail: pedro.navas@upm.es, d.manzanal@upm.es, angel.yague@upm.es

M.Molinos, M. M. Stickle and M. Pastor
Dep. Mathematics Applied to Civil Engineering, Technical Univ. of Madrid
E-mail: m.molinos@alumnos.upm.es, m.martins@upm.es, manuel.pastor@upm.es

the derivatives of the $u - p_w$ equations was necessary. This linearization was also made by Sanavia *et al.*[29] who considered several neglected terms of the previous works and extended the methodology to unsaturated soils [31].

By contrast, the complete formulation valid for all frequencies movements is known to be essential for solving dynamic problems [12,26]. Nevertheless, the formulation employing the total displacement of the water, U, as a nodal unknown is unstable when large deformations of the fluid phase occur. As an alternative, the employment of the relative water displacements, w, has been proved to be successful [15,18]. Traditional manner to solve the complete formulation is the utilization of implicit schemes [4,5,1,11] except the recent work of Ye *et al.* [33]. Thus, the current work represents the first one that solves the complete formulation with relative water displacements, $u - w$, using an explicit scheme. Since there is no necessity in formulating the tangent stiffness matrix in an explicit procedure, the complex process of linearization of the governing equations is avoided. In addition, as no matrix inversion is involved, the computational effort is minimized and code parallelization is facilitated.

Moreover, it bears emphasis that the proposed methodology, as it is thought for the finite strain regime, is carried out within a meshfree scheme due to its numerous advantages when large deformations are involved. In particular, the shape functions developed by Arroyo and Ortiz [2] based on the principle of maximum entropy [25] are employed. The spacial domain has been discretized into nodes and material points following the Optimal Transportation Meshfree (OTM) scheme of Li *et al.* [14]. The Drucker-Prager yield criterion, the good performance of which has been demonstrated for large deformation problems [?], is herein adopted.

In contrast to the work of Bandara and Soga [?] or Ceccato and Simonini [7], who made use of two material sets for solid and water phases in their Material Point Method (MPM) schemes, a single set of materials for the coupling between water and solid phases is employed in this work since the relative water displacement is considered. This leads to significant savings on the computational effort. In addition, this formulation is stronger than some others such as the Smooth Particle Hydrodynamics (SPH) since the pore pressure is also computed in the material points. The SPH formulation presents a tensile instability since only one nodal set is employed to contain displacement and stress fields.

The rest of the paper is organized as follows. The Biot's equations are presented next. The constitutive models employed to model the solid behavior are summarized in Section 3. The explicit methodology implemented is elucidated in Section 4. Applications to various problems are illustrated in Section 5. Relevant conclusions are drawn in Section 6. The definitions of all symbols used in the equations are provided in the nomenclature appendix.

2 Biot's equations: u-p_w formulation

The Biot's equations [3] are based on formulating the mechanical behavior of a solid-fluid mixture, the coupling between different phases, and the continuity of flux through a differential domain of saturated porous media. Hereinafter, the balance equations will be derived from Lewis and Schrefler [13] in the spatial setting (see [13] or [30,31] for the kinematic equations), departing from the more general equation, and, in order to reach the compact $u - p_w$ form, making the necessary hypotheses.

Concerning the notation, bold symbols are employed herein for vectors and matrices as well as regular letters for scalar variables. Let $\boldsymbol{u}$ and $\boldsymbol{U}$ represent the displacement vector of the solid skeleton and the absolute displacement of the fluid phase respectively. Since in porous media theory is common to describe the fluid motion with respect to the solid, the relative displacement of the fluid phase with respect to the solid one, $\boldsymbol{w}$, is introduced and expressed as [16]

$$\boldsymbol{w} = nS_w\left(\boldsymbol{U} - \boldsymbol{u}\right), \tag{1}$$

where S_w is the degree of water saturation and n the soil porosity. Note that $(\boldsymbol{U} - \boldsymbol{u})$ is usually termed as $\boldsymbol{u}^{ws}$ in the literature [13].

In the calculation of the internal forces of the soil, the Terzaghi's effective stress theory [32] will be followed, which is defined as follows:

$$\boldsymbol{\sigma} = \boldsymbol{\sigma'} - p_w\mathbf{I}, \tag{2}$$

where $\boldsymbol{\sigma'}$ and $\boldsymbol{\sigma}$ are the respective effective and total Cauchy stress tensors (positive in tension), whereas $\mathbf{I}$ is the second order unit tensor. Contrary, pore pressure p_w, is assumed positive for compression.

Let ρ, ρ_w and ρ_s respectively represent the mixture, fluid phase and solid particle densities, the mixture density can be defined as function of the porosity:

$$\rho = nS_w\rho_w + (1-n)\rho_s. \tag{3}$$

In the above equations, the porosity, n, is the ratio between the voids volume, V_v, and the total volume, V_T:

$$n = \frac{V_v}{V_T} = \frac{V_v}{V_v + V_s}, \tag{4}$$

where V_s is the volume of the solid grains.

In the current work, the soil is assumed to be totally saturated, i.e. V_v coincides with the water volume, which results S_w equals to one. Meanwhile, the volumetric compressibility of the mixture, Q [35] is calculated as

$$Q = \left[\frac{1-n}{K_s} + \frac{n}{K_w}\right]^{-1}, \tag{5}$$

where K_s is the bulk modulus of the solid grains, whereas K_w is the compressive modulus of the fluid phase (usually water).

Next, we first explain in detail the derivation of mass balance and linear momentum equations for a fluid saturated multiphase media. Then the final $u-p_w$ formulation is presented. The following equations are first given by Lewis and Schrefler [13]. In this research, D^s/Dt denotes the material time derivative with respect to the solid, considering:

$$\boldsymbol{a}^s = \ddot{\boldsymbol{u}} = \frac{D^s\dot{\boldsymbol{u}}}{Dt} = \frac{D^{2s}\boldsymbol{u}}{Dt^2}$$

$$nS_w\boldsymbol{a}^{ws} = \ddot{\boldsymbol{w}} = \frac{D^s\dot{\boldsymbol{w}}}{Dt} = \frac{D^{2s}\boldsymbol{w}}{Dt^2}$$

where $\boldsymbol{a}^s$ and $\boldsymbol{a}^{ws}$ are the solid acceleration and the relative water acceleration with respect to the solid respectively, being the proposed expressions based on the relationships $\dot{\boldsymbol{u}} \equiv \boldsymbol{v}^s$ and $\dot{\boldsymbol{w}} \approx nS_w\boldsymbol{v}^{ws}$.

2.1 Derivation of the mass balance equation

The general mass balance equation in a multiphase media for compressible grains is presented next. Let p_w, p_g represent the water and gas pressures respectively, T, the temperature, then this general mass balance equation is written as follows,

$$\left(\frac{\alpha-n}{K_s}S_w^2 + \frac{nS_w}{K_w}\right)\frac{D^s p_w}{Dt} + \frac{\alpha-n}{K_s}S_wS_g\frac{D^s p_g}{Dt} - \beta_{sw}\frac{D^sT}{Dt} + \left(\frac{\alpha-n}{K_s}S_wp_w - \frac{\alpha-n}{K_s}S_wp_g + n\right)\frac{D^sS_w}{Dt} + \alpha S_w\mathrm{div}\ \dot{\boldsymbol{u}} + \frac{1}{\rho_w}\mathrm{div}\ (\rho_w\dot{\boldsymbol{w}}) = -ne^w \tag{6}$$

where the right hand side term represents the quantity of water lost through evaporation for unit time and volume. The thermal expansion coefficient of the solid-fluid mixture, β_{sw}, is a combination of that of the solid, β_s, and the fluid, β_w:

$$\beta_{sw} = S_w[(\alpha-n)\beta_s + n\beta_w]. \tag{7}$$

In addition, α is the Biot's coefficient:

$$\alpha = 1 - \frac{K_T}{K_s}. \tag{8}$$

where K_T denotes the bulk modulus of the solid skeleton. Biot's coefficient may be usually assumed equal to one in soils as the grains are much more rigid than the mixture.

As we consider a totally saturated, iso-thermal multiphase media, $D^sT/Dt = 0, S_g = 0, S_w = 1, k^{rw} = 1, e^w = 0$, consequently, $D^sS_w/Dt = 0$. If additionally the fluid density variation is neglected and we take into consideration Eq. (5), Eq. (6) is simplified as,

$$\frac{\dot{p_w}}{Q} + \mathrm{div}\ \dot{\boldsymbol{u}} + \mathrm{div}\ \dot{\boldsymbol{w}} = 0, \tag{9}$$

2.2 Linear momentum balance equations

On the one hand, the relative velocity of the fluid, $\dot{\boldsymbol{w}}$, in Eq. (6) is defined through the generalized Darcy law as [13]

$$\dot{\boldsymbol{w}} = \frac{k^{rw}\boldsymbol{k}}{\mu_w}\left[-\mathrm{grad}\, p_w + \rho_w(\boldsymbol{g} - \ddot{\boldsymbol{u}} - \frac{\ddot{\boldsymbol{u}}}{n})\right], \tag{10}$$

where $\boldsymbol{g}$ represents the gravity acceleration vector, $\boldsymbol{k}$, the intrinsic permeability tensor of the porous matrix in water saturated condition, k^{rw} is the water relative permeability parameter (a dimensionless parameter varying from zero to one) and μ_w is the dynamic viscosity of the water [Pa $\cdot$ s]. For the case of isotropic permeability, the *intrinsic* permeability, expressed in [m^2], is related with the notion of hydraulic conductivity, κ [m/s], by the following equation

$$\frac{k}{\mu_w} = \frac{\kappa}{\rho_w g}. \tag{11}$$

On the other hand, according to Lewis and Schrefler [13], the linear momentum balance equation for the multiphase system can also be expressed as the summation of the dynamic equations for the individual constituents relative to the solid as, i.e.,

$$-\rho\ddot{\boldsymbol{u}} - \rho_w\ddot{\boldsymbol{w}} - nS_g\rho_g\boldsymbol{a}^{gs} + \mathrm{div}\ \boldsymbol{\sigma} + \rho\boldsymbol{g} = \boldsymbol{0}, \tag{12}$$

where the convective terms, related to the acceleration terms, have been neglected, which is normal in soils. Since in the present research there is no gassy phase, as the soil will be considered as totally saturated ($S_g = 0$), and plugging Eq. (2) into Eq. (12), the linear momentum equation can be written as follows

$$\mathrm{div}\ \left[\boldsymbol{\sigma'} - p_w\,\mathbf{I}\right] - \rho\ddot{\boldsymbol{u}} - \rho_w\ddot{\boldsymbol{w}} + \rho\boldsymbol{g} = \boldsymbol{0}. \tag{13}$$

2.3 The $u - p_w$ formulation

Considering the three Biot's equations, the $\boldsymbol{u} - p_w$ assumes that accelerations of the fluid phase are negligible. Thus, Eq. (13) yields:

$$\text{div}\ [\boldsymbol{\sigma'} - p_w\,\mathbf{I}] - \rho\ddot{\boldsymbol{u}} + \rho\boldsymbol{g} = \mathbf{0}. \tag{14}$$

Moreover, in order to avoid the employment of $\boldsymbol{w}$ as a degree of freedom of our problem, Eqs. (9) and (10) can be combined and the mass equation can be expressed as

$$\dot{p_w} = -Q\left[\text{div}\ \dot{\boldsymbol{u}} + \frac{\boldsymbol{k}}{\mu_w}\text{div}\left(\rho_w\boldsymbol{g} - \rho_w\ddot{\boldsymbol{u}} - \text{grad}\ p_w\right)\right]. \tag{15}$$

3 Constitutive models for the solid phase

In this Section, the hyperelastic and hyper-elastoplastic models, employed within this research, are outlined. Further information of both constitutive laws can be found in [19,24].

3.1 Neo-Hookean material model extended to compressible range

In this research, the Neo-Hookean constitutive behavior has been considered as a extension of the elastic one in the large strain regime. Moreover, among several variants, the one proposed by Ehlers and Eipper [11] has been chosen. This law takes into consideration the compaction point of the soil, from influence of the initial porosity n_0 and the Jacobian, i.e.

$$\boldsymbol{\tau}' = G(\boldsymbol{b} - \mathbf{I}) + \lambda\, n_0^2\left(\frac{J}{n_0} - \frac{J}{J - 1 + n_0}\right)\mathbf{I}, \tag{16}$$

where $\boldsymbol{\tau}'$ and $\boldsymbol{b}$ are the effective Kirchhoff stress tensor and the left Cauchy-Green tensor respectively, whereas J is the Jacobian determinant, G and λ are the Lamé constants.

3.2 Drucker-Prager yield criterion

In order to reproduce frictional-cohesive behavior at large strain, the traditional Drucker-Prager yield criterion [31,28] has been extended to large strain procedure. This methodology follows the work of Cuitiño and Ortiz [8] to relate the left Cauchy-Green strain tensor $\mathbf{b}$, calculated at the current configuration, and the small strain tensor $\boldsymbol{\varepsilon}$. Indeed, for the current loading step, $k+1$, the trial elastic deformations, pressure (p^{trial}_{k+1}) and the deviatoric stress tensor ($\mathbf{s}^{trial}_{k+1}$) are computed as the elastic deformations, pressure and the deviatoric stress tensor are computed as:

$$\mathbf{b}^{e\ trial}_{k+1} = \Delta\mathbf{F}^k\mathbf{b}^e_k(\Delta\mathbf{F}_k)^T, \tag{17}$$

$$\boldsymbol{\varepsilon}^{e\ trial}_{k+1} = \frac{1}{2}\log\mathbf{b}^{e\ trial}_{k+1}, \tag{18}$$

$$p^{trial}_{k+1} = K\,(\varepsilon^e_{vol})^{trial}_{k+1}, \tag{19}$$

$$\mathbf{s}^{trial}_{k+1} = 2G\,(\boldsymbol{\varepsilon}^e_{dev})^{trial}_{k+1}. \tag{20}$$

where K and G represent the bulk and shear moduli of the solid respectively. Regarding the Drucker-Prager yield criterion, the employed methodology allows to distinguish if the location of the stress state is on the cone or apex before calculating the plastic strain. The yield conditions for the classical and apex regions respectively are:

$$\begin{aligned} \Phi^{cl} &= \|\mathbf{s}^{trial}_{k+1}\| - 2G\Delta\gamma + 3\alpha_F[p^{trial}_{k+1} - 3K\alpha_Q\Delta\gamma] \\ &\quad -\beta c_{k+1}, \end{aligned} \tag{21}$$

$$\begin{aligned} \Phi^{ap} &= \frac{\beta}{3\alpha_F}\left[c_k + H\sqrt{\Delta\gamma_1^2 + 3\alpha_Q^2(\Delta\gamma_1 + \Delta\gamma_2)^2}\right] \\ &\quad -p^{trial}_{k+1} + 3K\alpha_Q\,(\Delta\gamma_1 + \Delta\gamma_2), \end{aligned} \tag{22}$$

where $\Delta\gamma_1 = \frac{\|\mathbf{s}^{trial}_{k+1}\|}{2G}$, $\Delta\gamma$ and $\Delta\gamma_2$ are the objective functions to be calculated in the Newton-Raphson scheme for the classical or apex regions accordingly. c_k is the cohesion of the material, H the hardening parameter and α_F,α_Q and β are material parameters that depend on friction and dilatancy angles as well as the shape of the yield surface, taking into account that the Drucker-Prager criterion employed a cone to approximate the Mohr-Coulomb surface and this cone can be outer or inner to the aforementioned surface (more information is found in [23]).

A limit value for the pressure, p_{lim}, is necessary to know which algorithm is to be employed. If the trial pressure is lower than this limit, classical return-mapping algorithm is employed, being this limit written as:

$$\begin{aligned} p_{lim} &= \frac{3\alpha_Q K}{2G}\|\mathbf{s}^{trial}_{k+1}\| \\ &\quad + \frac{\beta}{3\alpha_F}\left(\frac{\|\mathbf{s}^{trial}_{k+1}\|}{2G}H\sqrt{1 + 3\alpha_Q^2} + c_k\right). \end{aligned} \tag{23}$$

Te equivalent plastic strain, $\bar{\varepsilon}^p_{k+1}$, is calculated in different ways depending on the fact that if the stress state is in the classical or apex region as well:

$$\bar{\varepsilon}^p_{k+1} = \bar{\varepsilon}^p_k + \Delta\gamma\sqrt{3\alpha_Q^2 + 1}$$

$$\bar{\varepsilon}^p_{k+1} = \bar{\varepsilon}^p_k + \sqrt{\Delta\gamma_1^2 + 3\alpha_Q^2\,(\Delta\gamma_1 + \Delta\gamma_2)^2}$$

4 Discretization of the solution: Explicit scheme

To solve the aforementioned coupled problem in the time domain, the standard central difference explicit Newmark time integration scheme is employed. If the current time step is numbered as $k+1$, and assuming the solution in the previous step k has been already obtained (hence it is known), a relationship between $\mathbf{u}_{k+1}$, $\dot{\mathbf{u}}_{k+1}$ and $\ddot{\mathbf{u}}_{k+1}$ is established according to a finite difference scheme, as follows:

$$\begin{aligned}
\ddot{\boldsymbol{u}}_{k+1} &= \ddot{\boldsymbol{u}}_k + \Delta\ddot{\boldsymbol{u}}_{k+1}, \\
\dot{\boldsymbol{u}}_{k+1} &= \dot{\boldsymbol{u}}_k + \ddot{\boldsymbol{u}}_k\Delta t + \gamma\Delta t\Delta\ddot{\boldsymbol{u}}_{k+1}, \\
\boldsymbol{u}_{k+1} &= \boldsymbol{u}_k + \dot{\boldsymbol{u}}_k\Delta t + \frac{1}{2}\Delta t^2\ddot{\boldsymbol{u}}_k + \beta\Delta t^2\Delta\ddot{\boldsymbol{u}}_{k+1}.
\end{aligned} \tag{24}$$

Similarly, the pore pressure, evaluated at material point level, can be expressed in terms of its derivative.

$$p_{w_{k+1}} = p_{w_k} + \dot{p}_{w_k}\Delta t + \theta\Delta t\Delta\dot{p}_{w\,k+1}. \tag{25}$$

When the Newmark scheme parameters, γ and β are set to 0.5 and 0 respectively, the central difference scheme is obtained. In the present research, $\theta = \gamma = 0.5$. Rearranging terms, *Predictor* and *Corrector* terms can be obtained:

$$\dot{u}_{k+1} = \underline{\dot{u}_k + (1-\gamma)\Delta t\,\ddot{u}_k} + \gamma\Delta t\,\ddot{u}_{k+1}, \tag{26}$$

$$p_{w_{k+1}} = \underline{p_{w_k} + (1-\gamma)\Delta t\,\dot{p_w}_k} + \gamma\Delta t\,\dot{p_w}_{k+1}; \tag{27}$$

being the underlined terms the ones of the predictor step, which will be called $\dot{u}_{k+*}$ and $p_{w_{k+*}}$.

About the numerical stability of the proposed methodology, it is guaranteed when the Courant-Friedrichs-Lewy (CFL) condition is satisfied. In particular, the time step, Δt, should be small enough to ensure that the compressive wave can travel between nodes, i.e.

$$\Delta t < \frac{h}{V_c}, \tag{28}$$

where h represents the discretization size and V_c is the p-wave velocity (see [36]), which is defined by

$$V_c = \sqrt{\left(D + \frac{K_f}{n}\right)\frac{1}{\rho}}, \quad \text{where} \quad D = \frac{2G(1-\nu)}{1-2\nu}. \tag{29}$$

4.1 Spatial discretization

The Optimal Transportation Meshfree (CITAS) has been demonstrated to perform reasonably well in geotechnical problems and, specifically, in multiphase problems. CITASSSS It is based in the conjunction of material points and nodes. As mentioned before, the shape functions are based on the work of Arroyo and Ortiz [2], who defined the Local Max-Ent shape function (LME) of the material point (x) with respect to the neighborhood (x_a) as follows:

$$N_a(\mathbf{x}) = \frac{\exp\left[-\beta\left|\mathbf{x}-\mathbf{x_a}\right|^{\mathbf{2}} + \boldsymbol{\lambda}^*\cdot(\mathbf{x}-\mathbf{x_a})\right]}{Z(\mathbf{x},\boldsymbol{\lambda}^*(\mathbf{x}))}, \tag{30}$$

where the computation is done along a neighborhood N_b and

$$Z(\mathbf{x},\boldsymbol{\lambda}) = \sum_{a=1}^{Nb}\exp\left[-\beta\left|\mathbf{x}-\mathbf{x_a}\right|^2 + \boldsymbol{\lambda}\cdot(\mathbf{x}-\mathbf{x_a})\right]. \tag{31}$$

The first derivatives of the shape function can be obtained from the own shape function and its Hessian matrix $\mathbf{J}$ by employing the following expression:

$$\nabla N_a^* = -N_a^*\left(\mathbf{J}^*\right)^{-1}(\mathbf{x}-\mathbf{x_a}), \tag{32}$$

The parameter β defines the shape of the neighborhood and it is related with the discretization size (or nodal spacing), h, and the constant, γ, which controls the locality of the shape functions, as follows,

$$\beta = \frac{\gamma}{h^2}. \tag{33}$$

It bears emphasis that $\boldsymbol{\lambda}^*(\mathbf{x})$ comes from the minimization of the function $g(\boldsymbol{\lambda}) = \log Z(\mathbf{x},\boldsymbol{\lambda})$ to guarantee the maximum entropy. Moreover, in the remapping of the shape function, before recomputing the aforementioned minimization process, it is necessary to update the neighborhood and the parameter $\beta^p_{k+1} < \beta^p_k$ in order to improve the stability.

By employing the outlined shape functions and applying Galerkin procedure to the weak form of Eqs. (12) and (13) (See [31,28] for details), the following matrix equations appear:

$$\boldsymbol{R}^s - \boldsymbol{R}^w - \boldsymbol{M}^s\ddot{\boldsymbol{u}} + \boldsymbol{f}^{ext,\,s} = \mathbf{0} \tag{34}$$

$$-\boldsymbol{C}\dot{\boldsymbol{u}} + \boldsymbol{M}^w\ddot{\boldsymbol{u}} + \boldsymbol{f}^{ext,\,w} - \boldsymbol{R}^w = \dot{p_w} \tag{35}$$

where the internal and external forces are defined as:

$$\begin{aligned}
\boldsymbol{R}^s &= \sum_{P=1}^{N_P} V_P\boldsymbol{\sigma'}\nabla\mathbf{N} \\
\boldsymbol{R}^w &= \sum_{P=1}^{N_P} V_P p_w\nabla\mathbf{N} \\
\boldsymbol{f}^{ext,\,s} &= \boldsymbol{M}^s\boldsymbol{g} - \int_{\partial\Omega_\tau}\boldsymbol{\sigma'}\boldsymbol{n}\mathbf{N}d\Gamma \\
\boldsymbol{f}^{ext,\,w} &= \boldsymbol{M}^w\boldsymbol{g} + \int_{\partial\Omega_{p_w}} p_w\boldsymbol{n}\mathbf{N}d\Gamma,
\end{aligned}$$

and the mass and damping matrices, constructed as lumped matrices in order to alleviate the computational effort of the explicit scheme, are written as follows:

$$\boldsymbol{M}^s = \sum_{P=1}^{N_P} V_P \rho \mathbf{N}$$
$$\boldsymbol{M}^w = \sum_{P=1}^{N_P} Q\rho_w \frac{k}{\mu_w} V_P \mathbf{BmN}$$
$$\boldsymbol{C}^w = \sum_{P=1}^{N_P} Q V_P \mathbf{BmN}$$

being V_p and N_p the volume and the neighborhood of a material point P respectively, $\mathbf{B}$ the symmetric shape function gradient operator and $\mathbf{m}$ the identity matrix in Voigt notation. Thus, $\mathbf{Bm}$ reproduces the *divergence* operation.

4.2 Explicit integration

The proposed scheme seeks the value of the solid acceleration, $\ddot{\boldsymbol{u}}$, calculated from equation (34). It is worth mentioning that the subscript $k+1$ is employed for the current step and k in the previous one. Furthermore, in this calculation, it is necessary to predict the internal forces from the values of the predicted solid displacement, $\boldsymbol{u}_{k+*}$, and the predicted pore pressure, $p_{w_{k+*}}$. The stress has to be calculated in this predicted step as well:

$$\boldsymbol{\sigma'}_{k+*} = \boldsymbol{\sigma'}(\boldsymbol{F}_{k+*}) = \boldsymbol{\sigma'}(\boldsymbol{F}(\boldsymbol{u}_{k+*}))$$

Moreover, the approximation of the logarithmic strain as the measure to be employed in the reference configuration has been demonstrated to provide good performance when large deformations are modeled. (CITAS CUITIÑO; SANAVIA, TAMAGNINI). In the present research, the tensor $\mathbf{b}$, the Left Cauchy-Green strain tensor ($\mathbf{b} = \mathbf{F}\mathbf{F}^T$) depends on the displacement on the predicted step as follows:

$$\mathbf{b}_{k+*} = \mathbf{b}(\mathbf{F}_{k+*}) = \mathbf{b}(\mathbf{F}(\boldsymbol{u}_{k+*}))$$

Once the solid acceleration is reached, the pore pressure velocity can be calculated from Eq. (35). Also, in this equation, water internal forces and solid velocities have to be evaluated in the predicted step, $k+*$.

All these ingredients are those which integrate the Newmark Predictor-Corrector explicit algorithm for the $\boldsymbol{u}-p_w$ formulation at large strain. Its numerical implementation is explained in the following section.

4.2.1 Explicit algorithm within the OTM framework

The pseudo-algorithm of the whole model can be written as follows. The employment of the superscript p for material point calculations has to be pointed out.

1. Explicit Newmark Predictor ($\gamma = 0.5$, $\beta = 0$)
$$u_{k+1} = u_k + \Delta t \dot{u}_k + 0.5 \Delta t^2 \ddot{u}_k,$$
$$\dot{u}_{k+*} = \dot{u}_k + (1-\gamma)\Delta t\, \ddot{u}_k,$$
$$p_{w_{k+*}} = p_{w_k} + (1-\gamma)\Delta t\, \dot{p}_{w_k}.$$
2. Nodes and Material points position update
$$x_{k+1} = x_k + \Delta u_{k+1},$$
$$x^p_{k+1} = x^p_k + \sum_{a=1}^{Nb} \Delta u^a_{k+1} N^a(x^p_k).$$
3. Deformation gradient calculation and related parameters
$$\Delta \mathbf{F}_{k+1} = I + \sum_{a=1}^{Nb} \Delta u^a_{k+1} \nabla N^a(x^p_k),$$
$$\mathbf{F}_{k+1} = \Delta \mathbf{F}_{k+1} \mathbf{F}_k,$$
$$V = JV_0 = \det \mathbf{F}\, V_0,$$
$$n = 1 - \frac{1-n_0}{J}.$$
4. Update density and recompute lumped mass
$$\rho_{k+1} = n_{k+1}\rho_w + (1-n_{k+1})\rho_s.$$
5. Remapping loop, reconnect the nodes with their new material neighbors.
6. Constitutive relations from the Elasto-Plastic model, $\boldsymbol{\sigma'}_{k+*}$ and internal forces $\boldsymbol{R}^s_{k+*}$ and $\boldsymbol{R}^w_{k+*}$.
7. Calculate $\ddot{\boldsymbol{u}}_{k+1}$ from Eq. (34):
$$\ddot{\boldsymbol{u}}_{k+1} = [\boldsymbol{M}^s]^{-1} \left[\boldsymbol{R}^s_{k+*} - \boldsymbol{R}^w_{k+*} + \boldsymbol{f}^{ext,\,s}_{k+1}\right]$$
8. Calculate $\dot{p_w}_{k+1}$ from Eq. (35):
$$\dot{p_w}_{k+1} = -\boldsymbol{C}\dot{\boldsymbol{u}}_{k+*} + \boldsymbol{M}^w \ddot{\boldsymbol{u}}_{k+1} + \boldsymbol{f}^{ext,\,w}_{k+1} - \boldsymbol{R}^w_{k+*}$$
9. Explicit Newmark Corrector
$$\dot{u}_{k+1} = \dot{u}_{k+*} + \gamma \Delta t\, \ddot{u}_{k+1},$$
$$p_{w_{k+1}} = p_{w_{k+*}} + \gamma \Delta t\, \dot{p}_{w_{k+1}}.$$

5 Validation examples

This section is composed by two different problems. The first one deals with a consolidation, either pseudo-static or cyclic one, in order to validate the model in typical porous media applications. The second one, seeking the assessment of the performance of the proposed algorithm in a real geotechnical problem, studies the failure of a vertical wall of saturated soil.

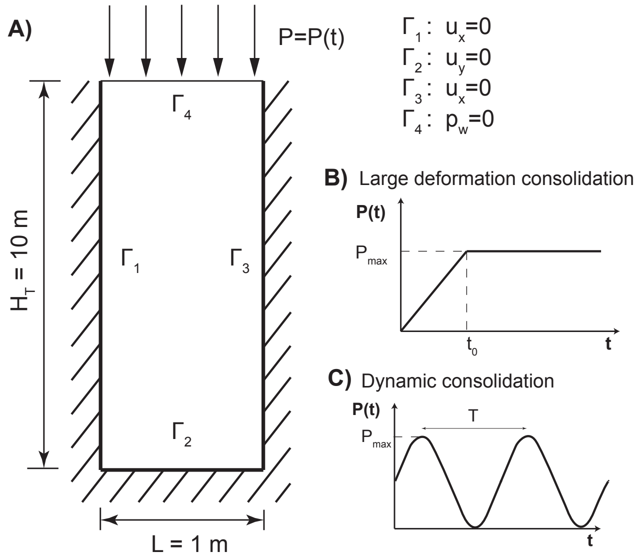

Fig. 1 A) Geometry and boundary conditions of the column of soil; Loading of B) large deformation consolidation and C) dynamic consolidation problems.

Table 1 Material parameters of the dynamic consolidation problem

λ [MPa]	29	K_w [MPa]	2.2×10^4
G [MPa]	7	K_s [MPa]	10^{34}
n	0.42	ρ_w [kg/m^3]	1000
k [m/s]	0.1	ρ_s [kg/m^3]	2700

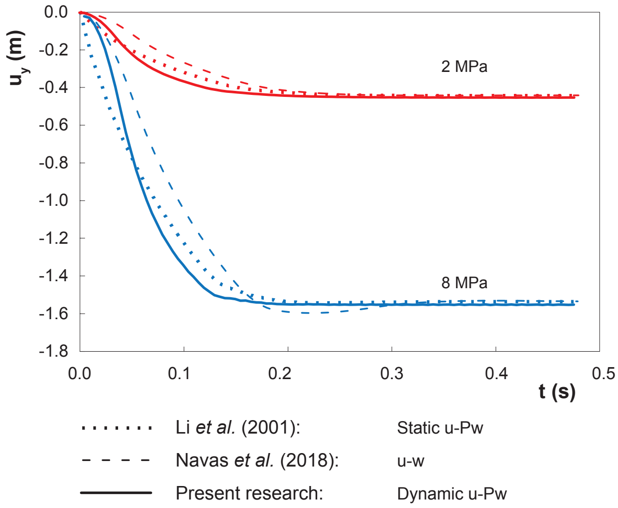

Fig. 2 Comparison between the settlement obtained by Li *et al.* [?], Navas *et al.* [23] and with the current methodology for the large deformation consolidation problem.

5.1 Consolidation of a column of soil

In the following two examples, an idealization of a semi-infinite stratum of soil through a 2D column is employed, which is a traditional procedure seen in the literature. This column has a height $H_T = 10m$ and a width $L = 1m$. Lateral movements are prevented as well as the vertical movement of the rigid base. On the top, the drainage is allowed ($p_w = 0$). This geometry and boundary conditions are depicted in Fig. 1. Also shape of both loads are depicted for the following problems, large deformation and dynamic consolidations, sections 5.1.1 and 5.1.2 respectively.

A regular nodal discretization of 0.5 m. size is employed, taking into account that the last top meter of the stratum is discretized with a 0.25 m. size in order to capture properly the wave provoked by the load. A similar mesh was proposed by Sabetamal *et al.* [27].

5.1.1 Large strain consolidation

Our goal in this section is the validation of the presented methodology when large deformation occurs. Taking this into consideration, the consolidation problem solved by Li *et al.* [?] is performed as a reference. The aforementioned geometry, seen in Fig. 1.A, is adopted. The column of soil is loaded following the curve of Fig. 1.B; increasing to reach P_{max} at $t_0 = 0.05$ s, when the pressure is kept constant until the end of the simulation (0.5 s). The soild and water parameters are listed in Tab. 1, being the Neo-Hookean material of Eq. (16) assumed in this case.

The validation is made against the solution proposed by Li *et al.* [?]. The settlement of the top surface along time is checked for two different values of P_{max}, namely 2 and 8 MPa, that provide two different scenarios, small and large deformation regimes. The obtained solutions are seen in Fig. 2 for the two cases. Three different solutions are depicted: Static $u - p_w$ (Li *et al.* [?]), Dynamic $u-w$ (Navas *et al.* [21]) and Dynamic $u-p_w$ (present research). At the final of the consolidation, similar values of the settlement are achieved. Since inertial terms are included in the proposed methodology, the comparison along the entire process described by Li *et al.* [?] is not possible, since in that research the quasi static $u - p_w$ formulation is assumed. Consequently, a ramped loading, contrary to the step-wise one employed in [?], is necessary in our case to avoid non-physical sudden loading. Similarly, the results are not comparable against the $u-w$ formulation since fluid acceleration, neglected in the present research, were considered. Because of this fact, in the $u - w$ solution, we can see that the settlement to reach values bigger than the final settlement between 0.18 and 0.3 seconds. It

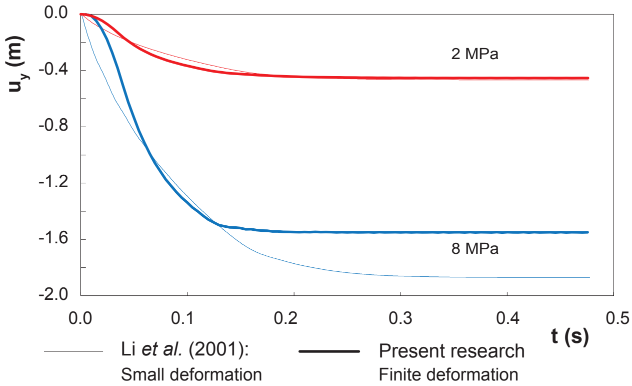

Fig. 3 Comparison between the settlement obtained with two different approached: large and small strain regimes.

Table 2 Material parameters of the and harmonic-loading consolidation problem.

E [MPa]	ν	K_w [MPa]	K_s [MPa]
30.0	0.20	$3.3{\cdot}10^8$	10^{34}
n	κ [m/s]	ρ_w [kg/m^3]	ρ_s [kg/m^3]
0.33	10^{-2}	1000	2000

is due to the fluid wave propagation, neglected in the present research.

Additionally, the obtained settlement is compared, for both loading states (2 and 8 MPa), against the small strain solution, which was provided also by Li *et al.* [?]. In Fig. 3 this comparison is plotted. As much is the deformation, as more important is the employment of the Finite Deformation regime since, as it is seen in this application, spurious results can be obtained.

5.1.2 Dynamic consolidation

Since soil inertial terms are considered in the proposed $u - p_w$ formulation, a dynamic problem has been proposed in order to see the performance of the proposed methodology. An interesting test was firstly studied by Sabetamal *et al.* [27] and later by Monforte *et al.* [17] and Navas *et al.* [20]. The material properties provided in table 2, and the sinusoidal load, shown in Fig. 1,C), are employed. In those researches, complete formulation ($u - w - p_w$ and $u - w$)results were provided. In this case, $u - p_w$ solutions of the pore pressure at different locations, for both stabilized and unstabilized, are presented against the stabilized $u - w$ one in Fig. 4. Slightly differences are encountered. Following, possible reasons are detailed.

On the one hand, the differences between the $u - w$ and $u - p_w$ solutions are small. This is due to the frequency of the load, which is not high enough to provoke water waves and, thus, the acceleration of the water phase can be neglected. Thus we have to take into account that, following the research of Zienkiewicz and coworkers [34], the configuration of this model lies on the denominated Zone I, where dynamic terms can be neglected (See point 1 of Fig. 5). This is the reason to have similar results for both $u - w$ and $u - p_w$ formulations.

Zones of Fig. 5 depend on the geometry, elastic properties, frequency of the load and permeability. By fixing the rest of the parameters and tuning the frequency from 25 to 200 (Point 2 in Fig. 5) and 500 Hz (Point 2 in Fig. 5), our problem becomes Zone II and III re-

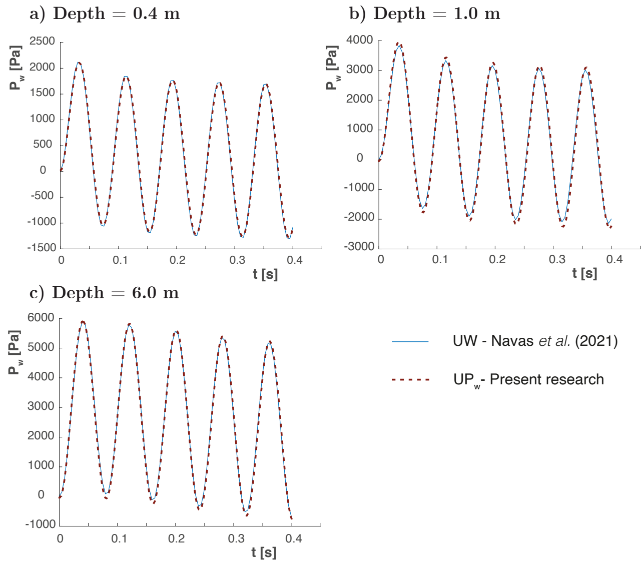

Fig. 4 Pore pressure evolution for the Harmonic-Loading consolidation problem at different depths a) 0.4 m. b) 1 m. and c) 6 m.

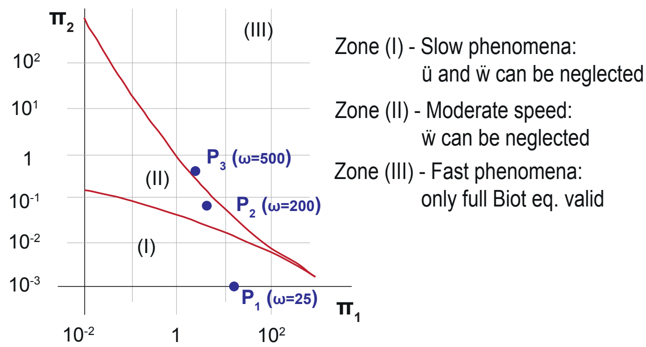

Fig. 5 Zones of the different behavior of the soil depending on the parameters Π_1 and Π_2 and values of ω and k for the different points to be studied.

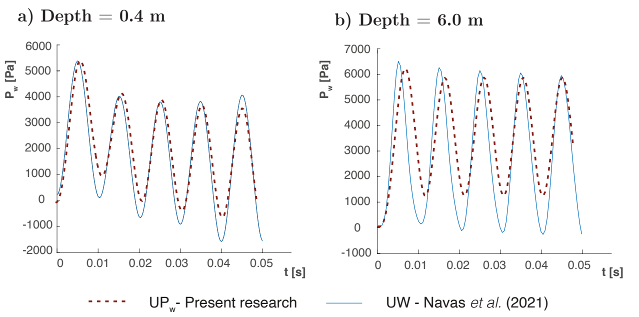

Fig. 6 Pore pressure evolution for the medium frequency Harmonic-Loading consolidation problem at different depths a) 0.4 m. and b) 6 m.

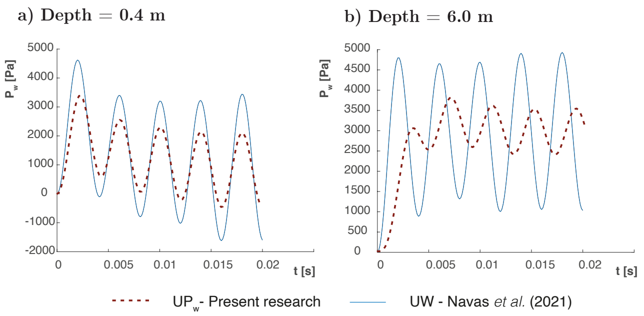

Fig. 7 Pore pressure evolution for the high frequency Harmonic-Loading consolidation problem at different depths a) 0.4 m. and b) 6 m.

spectively, where dynamic terms are important. Thus, in Figs. 6 and 7, the pore pressure evolution for both approaches is presented for 200 and 500 Hz. It is noticeable the difference, since the $u-p_w$ is not able to capture several peaks that the $u-w$ does, more displayed for 500 Hz. Indeed, differences are more severe when it is measured deeper in the column. It must be pointed out that, for 200 Hz, no differences should be found. However, the $u-p_w$ solution is not able to reach $u-w$. Although point 2 is close to the border of Zone III, the figure proposed by Zienkiewicz and coworkers [34] may be updated.

On the other hand, the second comparison is made in the settlement. In Sabetamal *et al.* [27] we find also the comparison against the analytical solution proposed by De Boer [9], corresponding to incompressible constituents. In Fig. 8 the settlement is plotted for the first 6 meters from the top in two instants: 0.135 s. and 0.155 s. There is a slightly difference between the peaks.

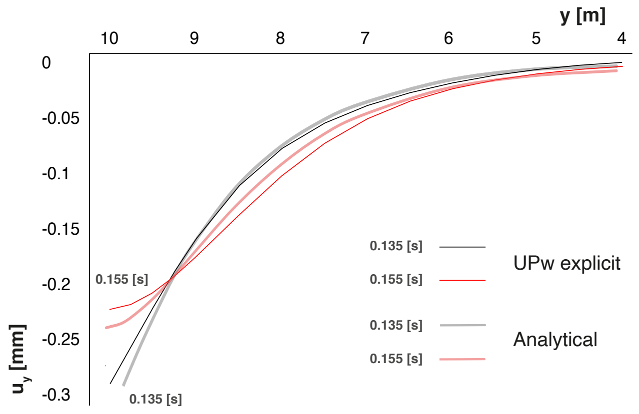

Fig. 8 Settlement in the Harmonic-Loading consolidation problem at two different instants: a) 0.135 s. and b) 0.155 s.

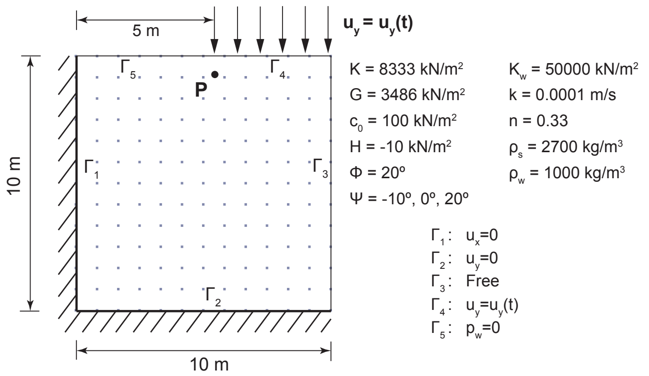

Fig. 9 Geometry, material parameters and boundary conditions of a square domain of water saturated porous material

5.2 Vertical cut

In this Section, the current methodology is applied the drainage of a square domain of saturated soil loaded on the top right half by a rigid footing. This load provokes the failure of the material in a typical vertical cut, whose shear band varies depending on the material properties. Precisely, the importance of this example lies in fact that, depending on the dilatancy angle, the formation of the shear band and the deformation pattern as well as the pore pressure may vary. For all the cases, the friction angle is kept at 20°.

The same problem was previously studied by Sanavia *et al.* [29,30] and Navas *et al.* [21,22] for both quasi static and dynamic regimes respectively. The geometry and material properties are shown in Fig. 9. A displacement of 1 m on the loaded boundary, Γ_4, is imposed gradually during the simulation, which has been fixed of 50 s. A regular 12x12 nodal discretization is employed, which corresponds to a nodal spacing of 0.833 m. The time step is of 5 ms.

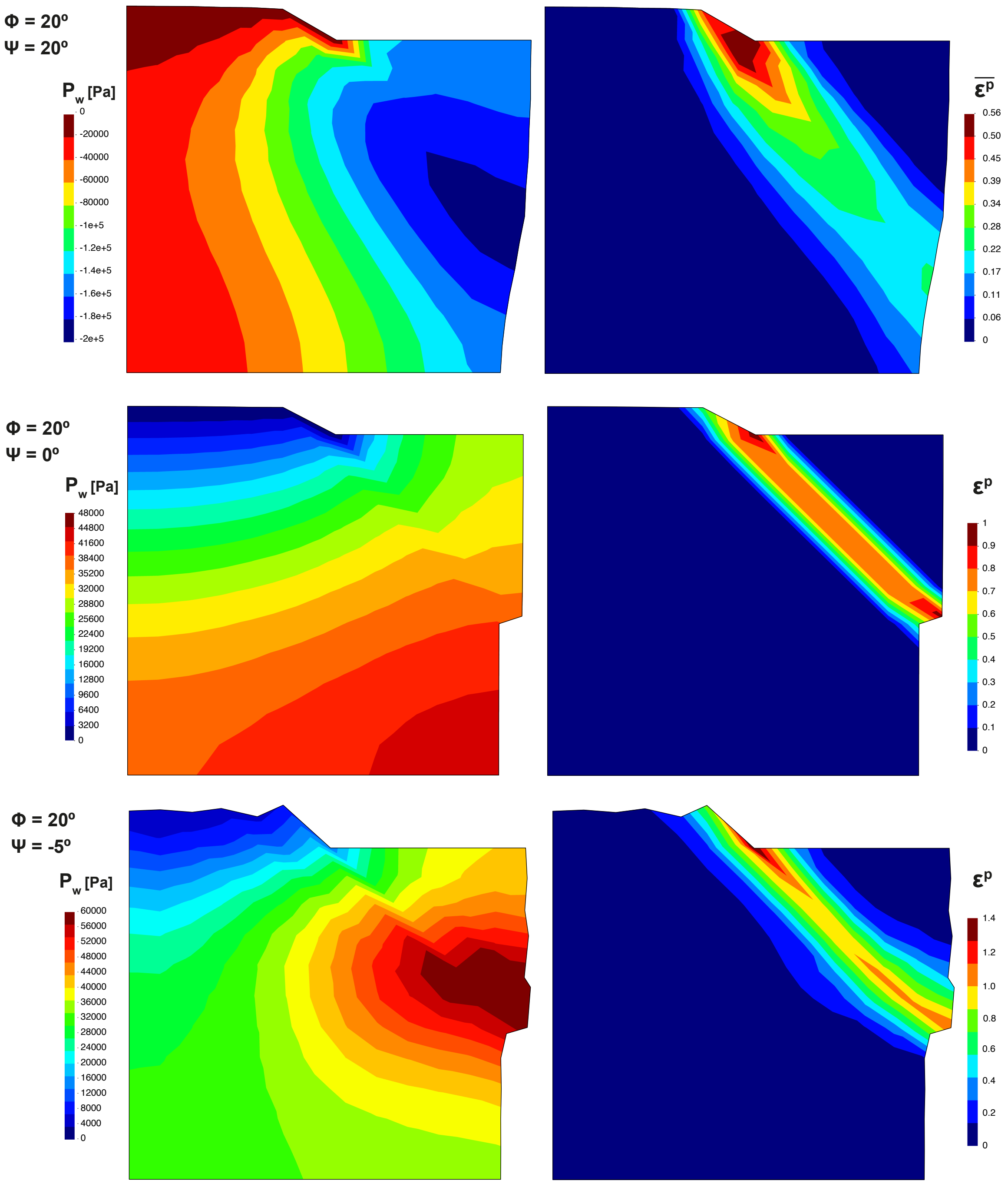

Fig. 10 Pore pressure (in Pa) and equivalent plastic strain at 50 s of the square domain for $\psi = 20°$, $\psi = 0°$ and $\psi = -5°$.

Results are depicted, at the final stage, in Fig. 10. In the referred bibliography we found similar distributions of pore pressure and plastic strain for dilatant, contractive or neutral soils. However, it is worth mentioning that those results were obtained with different coupled formulation, what leads to small difference of the obtained values. Despite this fact, the trend of the behavior of the soil is well captured.

About the shear band, it can be observed that there are no big variations on the obtained peak values of the equivalent plastic strain when the dilatancy angle changes, being slighlty bigger when the dilatancy angle decreases. However, an important decrease of the shear band slope is noticed when dilatancy decreases. For associate plasticity, $\psi = 20°$, the shear band almost reaches the toe of the lateral wall.

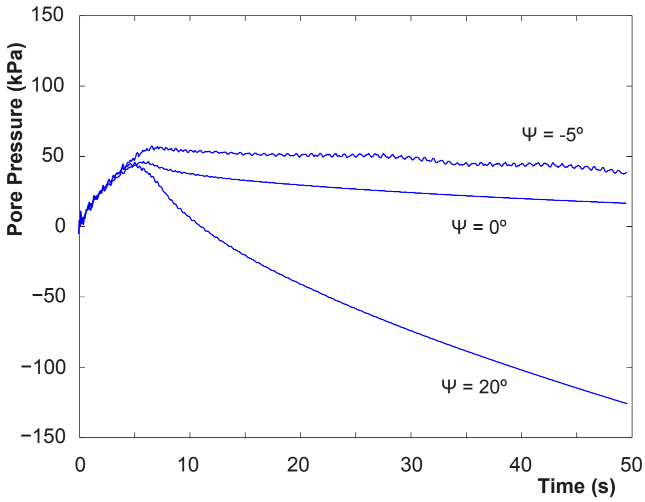

Fig. 11 Evolution of the pore pressure along the time in the point P.

In addition, the effect of the plastic dilatancy (contractancy) is evidenced by the negative (positive) pore pressure within the shear band zone (see Fig. **??**). Moreover, in the case of zero dilatancy angle, no marked pore pressure variation is observed within the shear band zone. Similar phenomena were obtained in the cited researches. In order to study the evolution of the principal results of the problem, the history of the pore pressure in a material point close to the shear band (Point P, see Fig. 9) have been depicted in Figs. 11.

For positive dilatancy values, smooth pore pressure evolution is observed. In addition, the peak pressure signals the initiation of plastic strain localization or shear band. The further extension of the shear band is accompanied by the continuous decreasing of the pore pressure. The material with dilatancy equal to 0° experiences a softer decreasing (close to a 0° slope), in this case, due to the dissipation of the pore pressure in the permeable boundary, not because of the shear band. From the same figure it can be seen a very unstable behavior of the soil of contractive angle. This happens since the soil does not admit more load: it is completely failed.

It must be pointed out that, in this research, the sought goal is the assessment of the performance of the proposed algorithm within this geotechnical problem. Other interesting studies of the performance of the Optimal Transportation Method were carried out in [21]. Of coarse, the influence of the size of the nodal discretization was important, getting, with a finer discretization, better resolution of the shear band and better pore pressure distribution. Also regular distributions provide better results. Finally, the importance of the neighborhood size was assessed, concluding that larger values of γ (which corresponds to smaller neighborhood) reduce the spurious smoothing out of the shear band, being the best results obtained for γ=1.4.

6 Conclusions

We have presented a new methodology to model bi-phase saturated soils, solving the coupled problem in an explicit manner. In this manuscript, the robustness of the proposed formulation is assessed, being this the main quality sought in an explicit bi-phase formulation. Moreover, several tools have been added to the methodology in order to be able to model very large strain geotechnical problems. Both elastic and plastic solid behaviors have been tested, meanwhile in the case of the water, the Darcy's law with solid inertial terms is is utilized. Also, this methodology has been carried out within the Local Max-Ent shape function, employing a spatial discretization based on the Optimal Transportation Meshfree scheme. Since the finite strain formulation is employed in order to be able to simulate large deformation regimes, advanced techniques such as any other meshfree scheme are well recommended.

Firstly, the performance of the method under large deformation regime is analyzed. The first example carried out is a large consolidation that was proposed firstly by Li *et al.* [**?**]. The behavior of the soil when the range of deformation is big is perfectly captured.

Secondly, the model is employed under high frequency loading conditions and an elastic media. The $u - p_w$ formulation behaves strong under low frequency loads, but is not well indicated when the frequency is bigger. The model is robust and captures both displacement and pore water pressure. Zones of applicability, proposed by Zienkiewicz *et al.* [36], may be revised in accordance to the results provided in this manuscript.

Finally, last example is performed within a Drucker-Prager flow rule in order to see the behavior of the pore pressure along the plastic shear bands depending on the dilatancy of the material based on the work of Sanavia *et al.* [30]. The obtained results are in accordance with the aforementioned research: contractive materials accumulate pore pressure while in the dilatant shear band the reduction of pore pressure is observed. Some pressure instabilities were found for contractive behavior, which is due to the breakage of the material, not allowing more load.

One of the main conclusions driven by the good performance of the proposed methodology is its extension to other particle based numerical techniques. Several researches of the author about the Material Point Method show the excellent fulfillment with Local Max-Ent shape function and an explicit predictor-corrector scheme, being both numerical techniques employed within this research. The robustness of the explicit scheme here presented encourage the authors to study other coupled formulations with similar integration schemes as well as the possibility of making dynamic relaxation techniques in order to extend the range of applicability to long simulations.

Acknowledgements This research was funded by the *Ministerio de Ciencia e Innovación*, under Grant Number, PID2019-105630GB-I00, which has been greatly appreciated. Authors would like to thank the administrative and technical support of the ETSI Caminos, Canales y Puertos, from the Universidad Politécnica de Madrid, as well. Additionally, the second author really appreciates the Entrecanales Ibarra Foundation for his undergraduate scholarship.

Conflict of interest

The authors declare that they have no conflict of interest.

Author contributions

Conceptualization and mathematical methodology, P. Navas and M. M. Stickle. Implementation, M. Molinos and P.Navas. Validation, A. Yagüe and D.Manzanal. Meanwhile supervision, project administration and funding acquisition belongs to M. Pastor. All authors have contributed to the writing and original draft preparation and they read and agreed to the published version of the manuscript.

Nomenclature

- $\boldsymbol{a}^s \equiv \ddot{\boldsymbol{u}}$: acceleration vector of the solid = material time derivative of $\boldsymbol{v}^s$
- $\boldsymbol{a}^{ws}$: relative water acceleration vector with respect to the solid = material time derivative of $\boldsymbol{v}^{ws}$ with respect to the solid
- $\boldsymbol{b} = \boldsymbol{F}\boldsymbol{F}^T$: left Cauchy-Green tensor
- $\overline{\boldsymbol{b}}$: body forces vector
- c: cohesion (equivalent to the yield stress, σ_Y)
- $\boldsymbol{C}$ (time integration scheme): damping matrix
- $\frac{D^s\square}{Dt} \equiv \dot{\square}$: material time derivative of $\square$ with respect to the solid
- $\boldsymbol{F} = \frac{\partial \boldsymbol{x}}{\partial \boldsymbol{X}}$: deformation gradient
- $\boldsymbol{g}$: gravity acceleration vector
- G: shear modulus
- h: nodal spacing
- H: hardening modulus, derivative of the cohesion against time.
- $\boldsymbol{I}$: second order unit tensor
- $J = \det\boldsymbol{F}$: Jacobian determinant
- k: intrinsic permeability
- $\boldsymbol{k}$: permeability tensor
- K: bulk modulus
- K_s: bulk modulus of the solid grains
- K_w: bulk modulus of the fluid
- $\boldsymbol{M}$: mass matrix
- n: porosity
- $N(\boldsymbol{x})$, $\nabla N(\boldsymbol{x})$: shape function and its derivatives
- p: solid pressure
- p_w: pore pressure
- $\boldsymbol{P}$ (time integration scheme): external forces vector
- Q: volumetric compressibility of the mixture
- $\boldsymbol{R}$: internal forces vector
- $\boldsymbol{s} = \boldsymbol{\sigma}^{dev}$: deviatoric stress tensor
- t: time
- $\boldsymbol{u}$: displacement vector of the solid
- $\boldsymbol{U}$: displacement vector of the water
- $\boldsymbol{v}^s = \dot{\boldsymbol{u}}$: velocity vector of the solid
- $\boldsymbol{v}^{ws}$: relative velocity vector of the water with respect to the solid
- $\boldsymbol{w}$: relative displacement vector of the water with respect to the solid
- $Z(\boldsymbol{x}, \boldsymbol{\lambda})$: denominator of the exponential shape function
- α_F, α_Q and β: Drucker-Prager parameters
- β, γ: time integration schemes parameters
- β, γ: LME parameters related with the shape of the neighborhood
- $\Delta\gamma$: increment of equivalent plastic strain
- $\bar{\varepsilon}^p$: equivalent plastic strain
- $\boldsymbol{\varepsilon}$: small strain tensor
- ε_0: reference plastic strain
- κ: hydraulic conductivity
- λ: Lamé constant
- $\boldsymbol{\lambda}$: minimizer of $\log Z(\boldsymbol{x}, \boldsymbol{\lambda})$
- μ_w: viscosity of the water
- ν: Poisson's ratio
- ρ: current mixture density
- ρ_w: water density
- ρ_s: density of the solid particles
- $\boldsymbol{\sigma}$: Cauchy stress tensor
- $\boldsymbol{\sigma'}$: effective Cauchy stress tensor
- $\boldsymbol{\tau}$: Kirchhoff stress tensor
- $\boldsymbol{\tau'}$: effective Kirchhoff stress tensor
- Φ: plastic yield surface
- ϕ: friction angle
- ψ: dilatancy angle

Superscripts and subscripts

- ^{dev}: superscript for deviatoric part

– ^{e}: superscript for elastic part
– $_k$: subscript for the previous step
– $_{k+1}$: subscript for the current step
– ^{p}: superscript for plastic part
– ^{s}: superscript for the solid part
– ^{trial}: superscript for trial state in the plastic calculation
– ^{vol}: superscript for volumetric part
– ^{w}: superscript for the fluid part relative to the solid one

References

1. Armero, F.: Formulation and finite element implementation of a multiplicative model of coupled poro-plasticity at finite strains under fully saturated conditions. Computer Methods in Applied Mechanics and Engineering **171**(3-4), 205–241 (1999). DOI 10.1016/S0045-7825(98)00211-4
2. Arroyo, M., Ortiz, M.: Local maximum-entropy approximation schemes: a seamless bridge between finite elements and meshfree methods. International Journal for Numerical Methods in Engineering **65**(13), 2167–2202 (2006). DOI 10.1002/nme.1534
3. Biot, M.A.: Theory of propagation of elastic waves in a fluid-saturated porous solid. I. Low-Frequency range. Journal of the Acoustical Society of America **28**(2), 168–178 (1956). DOI 10.1121/1.1908239
4. Borja, R.I., Alarcón, E.: A mathematical framework for finite strain elastoplastic consolidation. Part1: balance laws, variational formulation, and linearization. Computer Methods in Applied Mechanics and Engineering **122**(94), 145–171 (1995)
5. Borja, R.I., Tamagnini, C., Alarcón, E.: Elastoplastic consolidation at finite strain. Part 2: finite element implementation and numerical examples. Computer Methods in Applied Mechanics and Engineering **159**, 103–122 (1998). URL http://www.sciencedirect.com/science/article/pii/S0045782598801039
6. Cao, T.D., Sanavia, L., Schrefler, B.A.: A thermo-hydro-mechanical model for multiphase geomaterials in dynamics with application to strain localization simulation. International Journal for Numerical methods in Engineering **107**(January), 312–337 (2016). DOI 10.1002/nme
7. Ceccato, F., Simonini, P.: Numerical study of partially drained penetration and pore pressure dissipation in piezocone test. Acta Geotechnica **12**, 195–209 (2016)
8. Cuitiño, A., Ortiz, M.: A material-independent method for extending stress update algotithms from small-strain plasticity to finite plasticity with multiplicative kinematics. Engineering computations **9**, 437–451 (1992)
9. De Boer, R., Ehlers, W., Liu, Z.: One-dimensional transient wave propagation in fluid-saturated incompressible porous media. Archive of Applied Mechanics **63**(1), 59–72 (1993). DOI 10.1007/BF00787910
10. Diebels, S., Ehlers, W.: Dynamic analysis of fully saturated porous medium accounting for geometrical and material non-linearities. International Journal for Numerical Methods in Engineering **39**(1), 81–97 (1996). DOI 10.1002/(SICI)1097-0207(19960115)39:1¡81::AID-NME840¿3.0.CO;2-B
11. Ehlers, W., Eipper, G.: Finite Elastic Deformations in Liquid-Saturated and Empty Porous Solids. Transport in Porous Media **34**(1986), 179–191 (1999). DOI 10.1007/978-94-011-4579-4_11
12. Jeremić, B., Cheng, Z., Taiebat, M., Dafalias, Y.F.: Numerical simulation of fully saturated porous materials. International Journal for Numerical and Analytical Methods in Geomechanics **32**, 1635–1660 (2008). DOI 10.1002/nag.2347
13. Lewis, R.W., Schrefler, B.A.: The finite element method in the static and dynamic deformation and consolidation of porous media. John Wiley & Sons Ltd. (1998)
14. Li, B., Habbal, F., Ortiz, M.: Optimal transportation meshfree approximation schemes for fluid and plastic flows. International Journal for Numerical Methods in Engineering **83**(June), 1541–1579 (2010). DOI 10.1002/nme
15. López-Querol, S., Blázquez, R.: Liquefaction and cyclic mobility model in saturated granular media. International Journal for Numerical and Analytical Methods in Geomechanics **30**(5), 413–439 (2006). DOI 10.1002/nag.488
16. López-Querol, S., Fernández Merodo, J.A., Mira, P., Pastor, M.: Numerical modelling of dynamic consolidation on granular soils. International Journal for Numerical and Analytical Methods in Geomechanics **32**, 1431–1457 (2008). DOI 10.1002/nag
17. Monforte, L., Navas, P., Carbonell, J.M., Arroyo, M., Gens, A.: Low order stabilized finite element for the full Biot formulation in Soil Mechanics at Finite Strain. International Journal for Numerical and Analytical Methods in Geomechanics **43**, 1488–1515 (2019). DOI 10.1002/nag.2923
18. Navas, P., López-Querol, S., Yu, R.C., Li, B.: B-bar based algorithm applied to meshfree numerical schemes to solve unconfined seepage problems through porous media. International Journal for Numerical and Analytical Methods in Geomechanics **40**(6), 962–984 (2016). DOI 10.1002/nag.2472
19. Navas, P., López-Querol, S., Yu, R.C., Pastor, M.: Optimal transportation meshfree method in geotechnical engineering problems under large deformation regime. International Journal for Numerical Methods in Engineering **115**(10), 1217–1240 (2018). DOI 10.1002/nme.5841
20. Navas, P., Pastor, M., Yagüe, A., Martín Stickle, M., Manzanal, D., Molinos, M.: Fluid stabilization of the u-w biot's formulation at large strain. International Journal for Numerical and Analytical Methods in Geomechanics **Under review** (2020)
21. Navas, P., Sanavia, L., López-Querol, S., Yu, R.C.: Explicit meshfree solution for large deformation dynamic problems in saturated porous media. Acta geotechnica **13**, 227–242 (2018). DOI 10.1007/s11440-017-0612-7. URL https://doi.org/10.1007/s11440-017-0612-7
22. Navas, P., Sanavia, L., López-Querol, S., Yu, R.C.: u-w formulation for dynamic problems in large deformation regime solved through an implicit meshfree scheme. Computational mechanics **62**, 745–760 (2018). DOI 10.1007/s00466-017-1524-y. URL https://doi.org/10.1007/s00466-017-1524-y
23. Navas, P., Yu, R.C., Li, B., Ruiz, G.: Modeling the dynamic fracture in concrete: an eigensoftening meshfree approach. International Journal of Impact Engineering **113**, 9–20 (2018). DOI 10.1016/j.ijimpeng.2017.11.004
24. Navas, P., Yu, R.C., Ruiz, G.: SIMULATION OF MIXED-MODE FRACTURE IN CONCRETE THROUGH THE EIGENSOFTENING ALGORITHM.

Anales de Mecánica de la Fractura **35**, 393–398 (2018). DOI 10.1016/j.gaitpost.2016.12.006. URL http://www.researchgate.net/publication/235899988_Continuum_modelling_of_trap-affected_hydrogen_diffusion_in_hydrogen_assisted_fracture_analysis/file/e0b49529d924ac01fc.pdf
25. Ortiz-Bernardin, A., Puso, M.A., Sukumar, N.: Construction of Polygonal Interpolants: A Maximum Entropy Approach. International Journal for Numerical Methods in Engineering **61**(12), 2159–2181 (2004). DOI 10.1002/nme.1193
26. Ravichandran, N., Muraleetharan, K.K.: Dynamics of unsaturated soils using various finite element formulations. International Journal for Numerical and Analytical Methods in Geomechanics **33**, 611–631 (2009). DOI 10.1002/nag
27. Sabetamal, H., Nazem, M., Sloan, S.W., Carter, J.P.: Frictionless contact formulation for dynamic analysis of nonlinear saturated porous media based on the mortar method. International Journal for Numerical and Analytical Methods in Geomechanics **40**(1), 25–61 (2016). DOI 10.1002/nag.2347
28. Sanavia, L., Pesavento, F., Schrefler, B.A.: Finite element analysis of non-isothermal multiphase geomaterials with application to strain localization simulation. Computational Mechanics **37(4)**(4), 331–348 (2006). DOI 10.1007/s00466-005-0673-6
29. Sanavia, L., Schrefler, B.A., Stein, E., Steinmann, P.: Modelling of localisation at finite inelastic strain in fluid saturated porous media. Proc. In: Ehlers W (ed.), IUTAM Symposium on Theoretical and Numerical Methods in Continuum Mechanics of Porous Materials, Kluwer Academic Publishers pp. 239–244 (2001)
30. Sanavia, L., Schrefler, B.A., Steinmann, P.: A Mathematical and numerical model for finite elastoplastic deformations in fluid saturated porous media. In: G. Capriz, V. Ghionna, P. Giovine (ed.) Modeling and Mechanics of Granular and Porous Materials, Series of Modeling and Simulation in Science, Engineering and Technology pp. 297–346 (2001)
31. Sanavia, L., Schrefler, B.A., Steinmann, P.: A formulation for an unsaturated porous medium undergoing large inelastic strains. Computational Mechanics **28**(2), 137–151 (2002). DOI 10.1007/s00466-001-0277-8
32. Terzaghi, K.V.: Principles of Soil Mechanics. Engineering News-Record **95**, 19–27 (1925)
33. Ye, F., Goh, S.H., Lee, F.H.: A method to solve Biot's u-U formulation for soil dynamic applications using the ABAQUS/explicit platform. Numerical Methods in Geotechnical Engineering pp. 417–422 (2010). URL http://ahajournals.org
34. Zienkiewicz, O.C., Chan, A.H.C., Pastor, M., Paul, D.K., Shiomi, T.: Static and Dynamic Behaviour of Geomaterials: A rational approach to quantitative solutions. Part I: Fully saturated problems. Proc. Roy. Soc. Lond. **A429**, 285–309 (1990)
35. Zienkiewicz, O.C., Chan, A.H.C., Pastor, M., Schrefler, B.A., Shiomi, T.: Computational Geomechanics With Special Reference To Earthquake Engineering. Wiley (1999)
36. Zienkiewicz, O.C., Chang, C.T., Bettes, P.: Drained, undrained, consolidating and dynamic behaviour assumptions in soils. Géotechnique **30**(4), 385–395 (1980). DOI 10.1016/j.ocecoaman.2012.02.008
37. Zienkiewicz, O.C., Shiomi, T.: Dynamic Behaviour of saturated porous media: The generalized Biot formulation and its numerical solution. International Journal for Numerical and Analytical Methods in Geomechanics **8**(1), 71–96 (1984). DOI 10.1002/nag.1610080106